Domains in the low-temperature phase of magnetite from synchrotron-radiation x-ray topographs

C. Medrano*
ESRF, Boîte Postale 220, F-38043 Grenoble, France

M. Schlenker
Laboratoire Louis Néel du CNRS, Boîte Postale 166, F-38042 Grenoble, France

J. Baruchel
ESRF, Boîte Postale 220, F-38043 Grenoble, France

J. Espeso
Departamento de Física Moderna, Universidad de Cantabria, Santander, Spain
and ESRF, Boîte Postale 220, F-38043 Grenoble, France

Y. Miyamoto†
Saitama University, Urawa, Saitama 338, Japan
(Received 30 June 1998)

Domains in the low-temperature, ferrimagnetic, and ferroelectric, phase of magnetite Fe_3O_4 were investigated in the bulk, via their ferroelastic distortion, by means of synchrotron radiation x-ray topography, complemented by Nomarski optical microscopy on the surface. After cooling through the Verwey transition under a magnetic field parallel to [001], the images show a hierarchy of domains. Domains associated with a small difference in lattice distortion provide a clear indication that the symmetry is triclinic. They appear as a substructure of monoclinic domains separated by walls creating no long-range stress. The domain structure deduced from the observation, under the experimentally self-tested assumption that the walls involved are stress free, is favorable from the elastic, magnetostatic, and electrostatic points of view.
[S0163-1829(99)15201-9]

I. INTRODUCTION

Magnetite Fe_3O_4, the oldest magnetic material known, still contains riddles. It is ferrimagnetic, and known to undergo at 120 K the Verwey transition. From the magnetic point of view, this entails a change of easy magnetization directions from $\langle 111 \rangle$ at room temperature to near $\langle 001 \rangle$ at low temperature.[1] However, the distortion in the low-temperature phase is not tetragonal as would be expected just from magnetization along fourfold rotation axes of the cubic prototype phase, but apparently monoclinic.[2–5] Furthermore, detailed investigations have shown that magnetite is magnetoelectric, with spontaneous switchable electric polarization, hence ferroelectricity, combined with ferrimagnetism, and strongly suggest that the symmetry within one domain should in fact be triclinic.[6–9]

The present work is an attempt to shed some light on the symmetry through observations of the Bragg-diffraction images (x-ray topographs) of a single crystal, below the Verwey transition, under the influence of a magnetic field. We use the fact that symmetry lowering should bring about the coexistence of domains, with different spontaneous deformation states corresponding to different orientations of the low-temperature crystal axes. Our experimental approach combines the use of Nomarski optical microscopy of the specimen surface with x-ray Bragg diffraction imaging (often called x-ray topography) for the investigation of the bulk. The sensitivity of x-ray-diffraction imaging makes the detection of small differences in lattice distortion possible. With synchrotron radiation x-ray beams, this can be done in the white-beam form of topography, which is instrumentally simple and well suited to the application of controlled temperature and magnetic field, with intensity sufficient for real-time observations. Because the approach is not standard, we outline it first. We then present the sample and experimental setup, show the experimental results, and discuss them.

II. APPROACH

A. Search for symmetry using domains

The lowering of crystal symmetry associated with phase transitions leads to a distribution of domains, broadly called ferroelastic, or twins. When possible, the domains organize so that the distortion with respect to the high-symmetry phase is, within each of them, homogeneous and equal to the spontaneous distortion, but with different orientations. This implies that the walls separating them are coherent twin boundaries, or Nye walls, producing no long-range stress. The local symmetry is then the symmetry of the low-symmetry phase, and the geometrical transformations from one domain to another correspond to the symmetry elements lost in the transition.

If a technique sensitive enough to small lattice distortion can be used, the difference in distortion across the domains

will reveal the actual symmetry. X-ray Bragg diffraction imaging, i.e., x-ray topography, provides very high sensitivity to small differences in lattice distortion as well as images of the domains or walls. Early investigations of the simpler case of ferromagnetic domains showed that they are visible on x-ray topographs through their difference in (magnetostrictive) lattice distortion, described by the asymmetric tensor $\Delta u_{ij} \equiv \Delta(\partial u_i / \partial x_j)$ where **u** is the displacement, and **r**, with components x_j $(j=1,2,3)$, is the position vector.[10,11] Thus, the very observation of domain walls by x-ray topography can give indications about the symmetry.[12] A more quantitative approach involves measuring the difference in distortion between the domains, through the shift in the images in white beam.[13] In monochromatic beam the measurement of the effective misorientation between domains is, when the symmetry is known, a way to obtain, e.g., magnetostriction as a function of temperature.[14]

On general grounds of the minimum free-energy condition, it is expected that, whenever possible, domains tend to arrange so that their walls satisfy both the familiar magnetostatic condition (no magnetic charge distribution on the walls, i.e., conservation of the normal component of magnetization across the wall, hence no stray field), the electrostatic condition (the analogue of the previous one but with the electric polarization, if applicable) and an elastic compatibility condition. The latter can be expressed through quasi-dislocation densities associated with the wall,[15] in analogy with subgrain boundaries. The dislocation arrangements that produce no long-range stress (Nye walls in Kléman's terms) are favored. For such walls, each of the domains takes on the spontaneous deformation e^0_{ij} and compatibility is ensured by relative rotation around a direction contained in the wall.[15] Non-Nye walls imply inhomogeneous long-range strain, decreasing with distance from the wall with characteristic distances on the order of the crystal thickness or of the distance between walls. The condition for a wall to produce no long-range stress, i.e., to be a Nye wall, is equivalent to Sapriel's compatibility condition[16] which gives the equation of allowed walls as the solutions of

$$\Delta e^0_{ij} x_i x_j = 0, \tag{1}$$

where Δe^0_{ij} is the difference in spontaneous strain tensor between the two domains in some orthogonal coordinate system x_i. Equation (1) is representative of a cone. If $\det(\Delta e^0_{ij})=0$, it can be factorized into the product of two equations, corresponding to two mutually perpendicular planes. These walls can correspond to high-symmetry planes of the crystal (W walls in Sapriel's notation) or to walls whose orientation is determined by the particular values of Δe^0_{ij} (W' walls).

The Nye walls contain information about the symmetry because two different ferroelastic domains (i.e., domains differing in spontaneous strain tensor), A and B, have strain tensors related by a symmetry operation of the point group of the prototype phase, R_{ik}, which is lost during the transition:

$$e^0_{ij}(B) = R_{ik} e^0_{kl}(A) R_{jl}. \tag{2}$$

Magnetite has, at room temperature, point symmetry $m\bar{3}m$ if the distortion related to the magnetization along $\langle 111 \rangle$ is neglected. In the low-temperature phase, the point group is m or 1, corresponding to monoclinic or triclinic symmetry, respectively.[3,6]

The lattice parameters of the monoclinic structure have been measured by Yoshida and Iida,[3] whose convention for a, b, and c will be followed. We have not found any value of triclinic parameters in the literature. The diffraction spots and directions will, in this paper, be indexed in the cubic reference system u, v, w. For a domain where the monoclinic a axis is along [110], the b axis is along $[\bar{1}10]$, the c axis is along [001], and the nearly rhombohedral elongation of the low temperature phase along [111], the elements of the strain tensor, defined as $e(1)$, are related to the lattice parameters in the following way:

$$e^0_{uu} = \frac{1}{2}\left(\frac{a-\sqrt{2}a_c}{\sqrt{2}a_c} + \frac{b-\sqrt{2}a_c}{\sqrt{2}a_c} - \Delta\gamma \right),$$

$$e^0_{vv} = \frac{1}{2}\left(\frac{a-\sqrt{2}a_c}{\sqrt{2}a_c} + \frac{b-\sqrt{2}a_c}{\sqrt{2}a_c} + \Delta\gamma \right)$$

$$e^0_{ww} = \frac{c-a_c}{a_c}, \quad e^0_{uv} = \frac{1}{2}\frac{a-b}{\sqrt{2}a_c},$$

$$e^0_{vw} = \frac{1}{2}\left(\frac{\Delta\beta}{2} + \frac{\Delta\alpha}{2} \right), \quad e^0_{uw} = \frac{1}{2}\left(\frac{\Delta\beta}{2} - \frac{\Delta\alpha}{2} \right). \tag{3}$$

$\Delta\alpha$, $\Delta\beta$, and $\Delta\gamma$ are the deviations from 90°. The possibility of triclinic symmetry is allowed through $\Delta\alpha$ and $\Delta\gamma$. a_c is the cubic lattice parameter, whose exact value is not relevant since only differences between strain tensors, hence only a-b, a-$\sqrt{2}c$, $\Delta\beta$, $\Delta\alpha$, and $\Delta\gamma$, are involved.

The strain tensors corresponding to other domains will be called $e(j)$, the number j indicating the symmetry operations that have to be applied to the original strain tensor $e(1)$ to give the tensor $e(j)$, following the order of the International Tables for Crystallography[17] for space group $Fd\bar{3}m$ of the prototype phase, the translation part of the operations being disregarded since only the point-group symmetry is considered. In the case of monoclinic symmetry, 12 different strain tensors exist, each one associated to a monoclinic ferroelastic domain (MFD). They will be labeled $e(m)$, $m=1,\ldots,12$. Subsequent symmetry operations just reproduce one of the previous strain tensors, with for example $e(1)=e(14)=e(25)=e(38)$ all corresponding to the following operations: 180° rotation around the b axis, inversion and reflection on the ac mirror. We note that the Verwey transition is not a purely ferroelastic phase transition and other order parameters appear, breaking more symmetries. Thus the monoclinic point group would be m, with only an ac mirror,[3] and not $2/m$ as would be expected just from strain. In the case of triclinic symmetry the number of different strain tensors, or triclinic ferroelastic domains (TFD's) is 24. Thus $e(1)=e(25)$ and $e(14)=e(38)$ but now $e(1)\neq e(14)$, the only symmetry operation of the prototype phase which leaves the strain tensor invariant being the inversion. Each MFD can thus split into two TFD's.

The set consisting of a pair of spontaneous strain tensors and one of the allowed planes will be called a *twin*. It can be

labeled as i-j (opq), where the couple of numbers i-j corresponds to the strain tensors $e(i)$ and $e(j)$ which give rise to the twin, and (opq) is the wall orientation.

The classification of all possible twins shows that two cases have to be distinguished: (i) Some of the twins have a Δe^0_{ij} involving at least one of the monoclinic parameters (a,b,c or $\Delta\beta$) and at least one of the triclinic parameters ($\Delta\alpha$, $\Delta\gamma$). Since the latter are appreciably smaller than the former, $\Delta\alpha$ and $\Delta\gamma$ are not expected to have a big influence on the twin properties, and the approximation $\Delta\alpha=\Delta\gamma=0$, tantamount to considering a monoclinic twin, is permissible; (ii) In other twins Δe^0_{ij} depends only on $\Delta\alpha$ and $\Delta\gamma$. These are strictly triclinic twins. The involved domains are expected to be less misoriented than in the previous case. The W' walls of these twins have unknown orientation as $\Delta\alpha$ and $\Delta\gamma$ has not been measured yet. The strictly triclinic twins involve two strain tensors which would be equal in the case of monoclinic symmetry, such as $e(1)$ and $e(14)$. They can be seen as twins inside a MFD due to its splitting into two TFD's.

In this approach, the translation part of the symmetry operations is disregarded. In fact, the change in space-group symmetry $Fd\bar{3}m \rightarrow Cc$ implies the loss of translation elements:[4] the cubic face-centering translations, and the translation along one of the cubic axes $\langle 001\rangle$ due to doubling of the unit cell along the c axis. Thus, there could be domains related by some of these translations (antiphase domains, with identical reciprocal-lattice vectors). The phase shift induced by the translation faults in the field propagation inside the crystal can give rise to interference patterns on the topographs.[18–20] However, for the reflections allowed in the cubic phase (the only ones considered in this paper) there is no effect since the above translation vectors **f** would induce a phase shift $2\pi\mathbf{gf}=2\pi n$, where **g** is the diffraction vector, with n an integer. The experimental setup was specially sensitive to domain image splitting (see below), and interference phenomena are unlikely to be observed in the samples we used due to their moderate crystal perfection: indeed none of the section images we obtained showed Pendellösung fringes. This point will be discussed again in Sec. V.

Due to their relative misorientation, the domains will Bragg diffract a white beam of x rays into different directions. The next subsection describes the experimental arrangement to measure the splitting.

B. Specific experimental conditions

In a standard x-ray topographic approach based on laboratory generators, and in particular Lang's method, the photographic film or plate is placed as close as possible to the specimen to minimize image blurring in the divergent x-ray beam. Therefore, small changes in the direction of the diffracted beam are not visible, and the image is considered to be the projection of the distribution on the exit face of the crystal of the diffracted beam intensity. Contrast is then due to changes in the wave-field propagation entailed by the defects in the almost perfect single crystal, and usually described by the dynamical theory of diffraction. Because these effects are significant only in the plane of incidence, consideration is restricted to this plane.

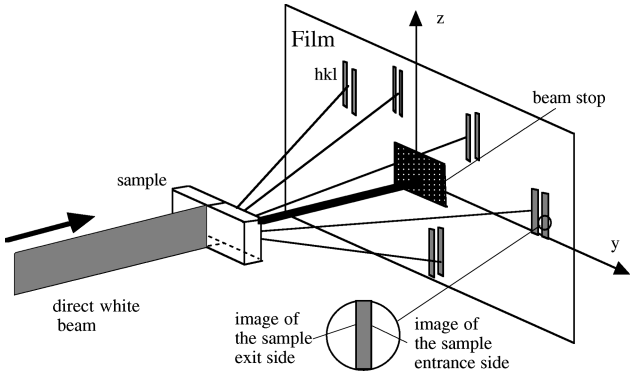

FIG. 1. Experimental setup for white beam section topography showing schematically the splitting in *hkl* reflections (due to the presence of domains in the sample). The inset shows the usual view of an individual section image, whose sides correspond to the exit and entrance sides of the sample.

The situation is different at third-generation synchrotron radiation sources, characterized by very small sizes of the electron beam producing the radiation. On beamline ID19 of ESRF used in the present experiments, the divergence of the white x-ray beam is 10^{-6} rad, and setting the film at a distance $d=45$ cm results in a geometrical blurring of only 0.45 μm. On the other hand, a rotation by 10^{-4} rad of the diffracting planes, or equivalently of the diffraction vector, results in a shift in the image by 90 μm, and both the displacements parallel and perpendicular to the scattering plane are effective.

Thus, an experimental arrangement in which a low-divergence white x-ray beam is diffracted by the stationary crystal, i.e., a Laue pattern, can provide a combination of (direct space) shape and position information about the domains and of (reciprocal-space-type) information about the variation in lattice distortion, revealed through the splitting of the Bragg-diffraction (topographic) images. The use of a large crystal-film distance improves the sensitivity to this splitting (reciprocal space information), while the image visibility (direct space information) improves at smaller distances.

Although the overall view of the domain structure could be expected to show up better on images of the whole sample, i.e., projection topographs,[21] the complexity of the situation prevailing in the fairly thick sample that was mostly investigated made section topography more informative. In this approach,[22] the beam is restricted to a blade shape by a slit, and the region sampled is, to a good approximation, the intersection of the crystal by the virtual blade. The splitting component perpendicular to the slit image was measured in each case for several Bragg reflections, corresponding to different wavelengths (Fig. 1). The next subsection describes the procedure used for analyzing the image splitting.

C. Analysis of the image separation

The position of a Laue spot on the film, set perpendicular to the incident white beam, can be expressed as a function of the diffraction vector **g** as

$$\frac{y}{d}=-2\frac{g_x g_y}{g_x^2-g_y^2-g_z^2},$$

$$\frac{z}{d} = -2\frac{g_x g_z}{g_x^2 - g_y^2 - g_z^2}, \tag{4}$$

where the x axis is antiparallel to the direct beam, the y and z axis are film coordinates perpendicular to it, and d is the crystal-to-film distance.

If two domains have a difference in **g** vector $\Delta\mathbf{g}$ they produce images whose separation is

$$\frac{\Delta y}{d} = \frac{2g_y g^2 \Delta g_x - 2g_x(g_x^2 + g_y^2 - g_z^2)\Delta g_y - 4g_x g_y g_z \Delta g_z}{(g_x^2 - g_y^2 - g_z^2)^2},$$

$$\frac{\Delta z}{d} = \frac{2g_z g^2 \Delta g_x - 4g_x g_y g_z \Delta g_y - 2g_x(g_x^2 - g_y^2 + g_z^2)\Delta g_z}{(g_x^2 - g_y^2 - g_z^2)^2}. \tag{5}$$

On the other hand, $\Delta\mathbf{g}$ is a function of the tensor $\Delta u_{ij} = \Delta(\partial u_i / \partial x_j)$ where **u** is the displacement:[23]

$$\Delta g_i = -\Delta u_{ji} g_j . \tag{6}$$

The condition of no long-range stress from a (Nye) wall implies that there are only three nonzero components of Δu_{ij}:[14,15]

$$\Delta u_{13} = 2\Delta e_{13}^0,$$

$$\Delta u_{23} = 2\Delta e_{23}^0, \tag{7}$$

$$\Delta u_{33} = \frac{C_{11} - C_{12}}{C_{11}}\Delta e_{33}^0,$$

where the x_3 axis is perpendicular to the wall, x_1 and x_2 are in the wall and the C_{ij} are the elastic constants.

The geometry of the sample in the x-y-z reference system is known through the indexing of the Laue pattern, performed using the OrientExpress computer program.[24] This is equivalent to the knowledge of g_i for all the spots.

The most general procedure to analyze the image separation proceeds as follows:

(1) The image separation on the film is measured, yielding a set of data $\Delta y/d, \Delta z/d$ as a function of the spot's indices hkl.

(2) One of the allowed Nye type walls is chosen, which sets the reference system linked to the wall, i.e., the x_1, x_2, and x_3 axes.

(3) After suitable changes in coordinate system, the values of Δg_i are expressed as a function of only three parameters: Δu_{13}, Δu_{23}, and Δu_{33}. If the particular twin under consideration implies one of them to be zero (or some relation between them), or if the selected spots are not sensitive to some of them, a further reduction in the number of free parameters is obtained.

(4) The data $\Delta y/d$ and $\Delta z/d$ can then be fitted with these three parameters using formulas (5) through a standard least-squares procedure. Since the sign of the separation is usually undetermined, the fit was often performed on the separation squared.

Two criteria determine whether the tentatively chosen twin is responsible for the observed images:

(i) The fit should account for the dependence on the spot position or indices, and it should not deviate too much from the experimental values.

(ii) The values of Δu_{13}, Δu_{23}, and Δu_{33} obtained from the fit can be compared to the published values of the lattice parameters, since they should fulfill formula (7) for the given twin, the strain tensor being related to the lattice parameters as shown above.

Some of the spots should show no image splitting for a given twin. This provides a selection rule allowing some of the twin possibilities to be disregarded without calculations. It is emphasized that the condition that the walls produce no long-range stress is experimentally self-tested if the image does not feature streaks.

III. SAMPLE AND EXPERIMENTAL SETUP

The samples were single-crystal plates of magnetite Fe_3O_4 grown from 99.99% Fe_2O_3 in a mixture of CO and CO_2 gases by the Bridgman method, mechanochemically polished, with their main surface parallel to $(1\bar{1}0)$. Most of the x-ray imaging results shown were obtained on a sample 0.77 mm thick and of size about 7×5 mm^2 and, unless stated explicitly, the discussion will center on this. However, a topographic investigation was also carried out on a specimen 0.18 mm thick, while the Nomarski optical microscopy experiments were performed on a sample 1.3 mm thick and with surface about 4.4×4.6 mm^2.

The x-ray-diffraction imaging experiments were performed on the imaging and high-resolution diffraction beamline ID 19 at the European Synchrotron Radiation Facility (ESRF) in Grenoble, France. ID 19 uses the beam produced by an 11-pole wiggler, 145 m from the sample position. The sample was cooled in a helium closed-circuit refrigerator (''Displex'') or in an ILL-type ''orange cryostat.'' The temperature in the Displex could not be measured accurately since the thermometer is placed on the cool finger and the white synchrotron radiation beam, in spite of filtering, delivers a sizeable heat load on the sample. A magnetic field of up to 400 mT could be applied. The diffraction spots were monitored using two television cameras. One of them, with a broad field of view, indicated the excitation of the reflections and the position of the beams, hence essentially gave a reciprocal-space view. The other was a high-sensitivity Sofretec camera system with 40 μm resolution, involving the observation, via a mirror set at 45° to the diffracted x-ray beam, of the visible-light image provided by a thin scintillator. It allowed the development of the transition and the changes produced by the magnetic field to be followed in real time. The pictures were recorded on Kodak SR radiographic film, usually placed at a distance of about 45 cm from the sample. Exposures times were between 1 and 30 s.

As mentioned above, the projection topographs, made by illuminating the whole sample, provide an overall view, where it is however difficult to disentangle the effect of the various domains in the sample. Therefore most of the information was obtained from section topographs, made with the white beam restricted by a slit 20 or 40 μm in width, set vertically, i.e., almost parallel to [110]. Then only a small volume of the specimen is investigated at a time, and the displacements between images are readily related to the dif-

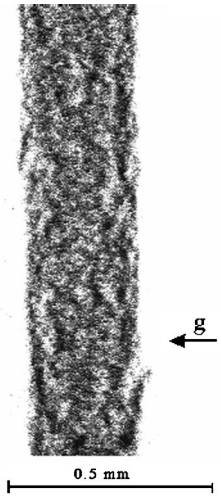

FIG. 2. White beam vertical section topograph at room temperature in the magnetically saturated state. Reflection $1\bar{1}11$, $\lambda = 0.34$ Å, absorption factor $\mu t \approx 1.5$.

ference in distortion in the locally coexisting domains. The component of this displacement perpendicular to the slit image was measured.

Observations on the surface of a sample with the same $(1\bar{1}0)$ orientation, but thickness 1.3 mm were performed in the low-temperature phase using a Nomarski interference microscope. In this device, based on a quartz prism placed between a polarizer and an analyzer, the phase difference between reflected rays are converted into intensity variations. Microsteps less than a nm high and rooflike deviation of the surface in adjacent domains, with slopes on the order of 10^{-4} rad, can be detected. The orientation of the magnetic field, provided by an electromagnet and with maximum intensity 420 mT, with respect to the sample could be changed by rotating the cryostat around its axis. The Nomarski images were monitored through a CCD camera and recorded on video tapes. Photographs were taken with a 35 mm camera.

IV. EXPERIMENTAL RESULTS

The low-temperature phase was investigated in three different situations: case I corresponds to cooling through the Verwey transition in zero field; case II to cooling in zero field and application of a magnetic field in the low-temperature phase; case III to cooling in a magnetic field. The field was applied along [001] to within 15°.

Figure 2 shows a section topograph taken at room temperature, in the magnetically saturated state. Many nonmagnetic defects are observed, making the observation of small domains in the low-temperature phase difficult.

Several well-separated images appear when the sample goes through the transition in zero field (case I, Fig. 3). Seven are visible in some spots. An essential point in unraveling the splitting is the fact that the lower parts of some of these images are correlated: image *C* could be obtained from image *D* just by applying a translation while images *A* and *B* are complementary: thus, a careful analysis of them indicated to us that following the coordinate parallel to the slit, the existence of a black spot in *A* coincides with a white space in *B*. The lower part of the sample shows some streaks between

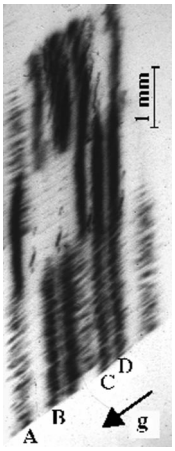

FIG. 3. White beam vertical section topograph in case I (cooling in zero field). Reflection $33\bar{5}$, $\lambda = 0.25$ Å, $\mu t \approx 0.5$, $T \approx 30$ K.

the main images corresponding to distorted regions. This is taken to indicate that the domain arrangement is not compatible from the elastic point of view, at least at some level of the structure. A hierarchy of domains appears, with domains well separated in Bragg angle and domains less separated. The latter induce a broad image, which is in fact related neither to the slit width nor to the crystal thickness, and is due to the dispersion in Bragg angle. No spatial information, apart from the correlation between the images, could be extracted, even with images taken at smaller crystal to film distances. Setting the film parallel to the incident beam, in order to increase the section image size, did not result in improved legibility either, because the images were severely broken up. The reasons of the bad image visibility are (i) the intrinsic defects and (ii) the very probable presence of very small domains (<5 μm) giving the already mentioned high image width. The main features (existence of several well separated images and streaks) are reproducible in different runs, but the volume distribution in the sample is not. No changes were observed down to 30 K in the main images, at least as seen on the Sofretec camera.

If a field is applied to the sample after cooling in zero field (case II) an abrupt change in domain arrangement occurs for a field between 80 and 225 mT, with the exact value being irreproducible. This corresponds to axis switching, i.e., the change of the *c* axis from one of the cube edges ([100] or [010]) to that parallel to the magnetic field, [001]. The number of domains is decreased and better defined images are obtained (Fig. 4). Further variations in field (from $+400$ to -400 mT) or in temperature (down to 4.2 K), induced no further domain change, at least as seen on the display from the Sofretec camera. The domain structure in this case is highly nonreproducible, as the examples of Figs. 4(a) and 4(b) show.

In case III, a 300 mT field was applied during cooling, and increased to 400 mT during the coexistence of the high- and low-temperature phases. As in case II, field or temperature (down to 4.2 K) variations did not change the appearance of the images on the Sofretec camera once the transition was passed. The observed images are angularly less separated than in the previous cases. There are always four images, which can be grouped into two couples: 1-2 and 3-4 (Fig. 5). Images 3 and 4 are only distinguishable on high

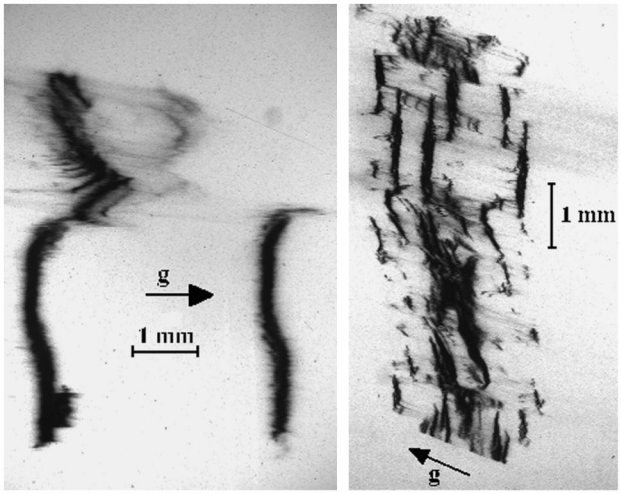

FIG. 4. White beam vertical section topograph in case II (application of magnetic field ∥ [001] after cooling in zero field): (a) Reflection 004, $\lambda = 0.45$ Å, $\mu t \approx 2.5$, $T \approx 30$ K; (b) 206, $\lambda = 0.35$ Å, $\mu t \approx 1$, $T = 110$ K. (a) and (b) correspond to two different runs.

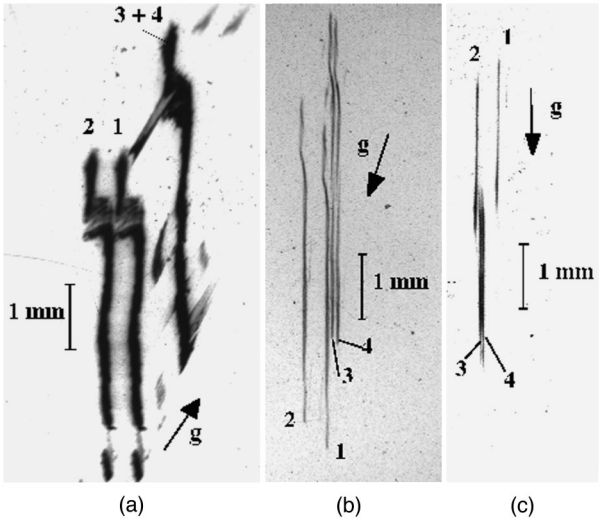

FIG. 5. White beam vertical section topograph in case III (cooling through the Verwey transition in magnetic field ∥ [001]). (a) Reflection 222, $\lambda = 0.47$ Å, $\mu t \approx 2.5$, $T = 110$ K, $B = 300$ mT; (b) Reflection $\overline{5}\overline{9}3$, $\lambda = 0.3$ Å, $\mu t \approx 1$, $T = 110$ K, $B = 300$ mT; (c) Reflection 862, $\lambda = 0.23$ Å, $\mu t \approx 1$, $T = 110$ K, $B = 0$. (a) and (b) correspond to the same run.

Bragg angle reflections. Images 1 and 2 seem to be copies, just translated, of each other, and so do images 3 and 4. The volume distribution changes from one experiment to another. In Figs. 5(a) and 5(b) the four images cover the whole sample, while in Fig. 5(c), corresponding to a different run, couple 1-2 is in the upper part of the sample and couple 3-4 in the lower one.

A thorough analysis was performed for case III. The lack of streaks between the main images in this case indicates an elastically good domain arrangement (Nye walls). Thus the approach outlined in Sec. II can be used to study the four images in Figs. 5(a) and 5(b). They are taken to correspond to monoclinic twins since they are well separated, and it is assumed that all the domains involved have the *c* axis close to [001] since the magnetic field was applied along this direction. The results of the analysis, performed as outlined in Sec. II C, of the separation between these four images, except between images 3 and 4, are summarized in Table I, with the indication of the twin assignment for the observed images.

A clear graphical view of the validity of the fit can be obtained. At the largest crystal-to-film distance (45 cm), only one Laue circle, *kkl* in the axis convention used, was recorded. The ratio k/l determines the spot position, hence the image separation can be represented as a function of k/l (Fig. 6). A very good agreement is found. Couple 3-4 is not separated on the *kkl* circle and only the images corresponding to large Bragg angle spots, recorded with the film close to the sample, show visible image separation. The calculations show that only one of the monoclinic twins fulfills these conditions. It is the twin 3-4 (001).

These large Bragg angle spots also reveal an internal structure (Fig. 7). In spite of the existence of four separated images, the standard view of a section topograph as describing the defect distribution along the depth of the sample (spatial information) can be applied within each individual image. Bands are observed at 42° (after correction for projection effects) from the vertical direction, which is very close to [110]. Figures 7(a), 7(b), and 7(c) correspond to the same spot but with different crystal-film distances. The set of bands seems to be less tight at higher distances. In addition,

TABLE I. Twins associated with the images of Figs. 5(a) and 5(b) and relations between the parameters obtained from the fits to the experiment and those found in the literature. Strictly, the walls allowed between 1–3 and 2–4 are not (101) type but are $(e^0_{uv},0,e^0_{uw})$ type. However, since the distortion is close to trigonal, $e^0_{uv} \cong e^0_{uw}$.

Domains	Wall	Twin	Fit shown in figures	Lattice parameter from present fit, $T = 110$ K	Lattice parameter from Yoshida and Iida (Ref. 3) ($T = 100$ K)
1-2	(001)	1-2 (001)	Fig. 6(a)	$\Delta\beta(\text{deg}) = 0.22\,(2)°$	0.23°
1-3	(101)	1-3 (101)	Fig. 6(b)	$\frac{1}{2}\frac{a-b}{a} + \frac{\sqrt{2}\Delta\beta}{4} = 0.0036\,(2)$	0.003
2-4	$(10\overline{1})$	2-4 $(10\overline{1})$	Fig. 6(c)	$\frac{1}{2}\frac{a-b}{a} + \frac{\sqrt{2}\Delta\beta}{4} = 0.0030\,(2)$	0.003

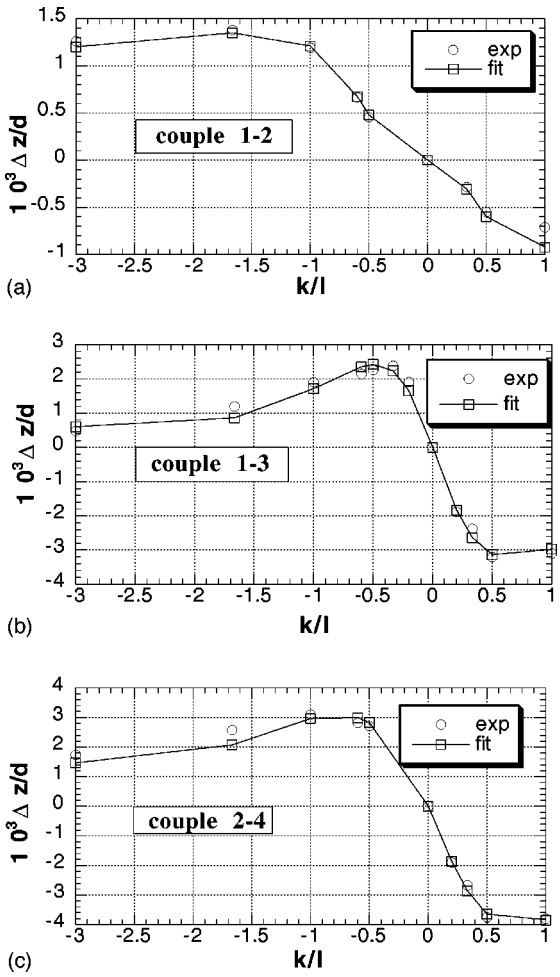

FIG. 6. Fitted values (fit) to the measured image separation (exp) as a function of k/l. Figure 5(a) corresponds to the experiment where these results were obtained. Lines joining the fitted points are guides to the eye.

couple 1-2 shows striations parallel to **g** [see the magnified view in Fig. 7(d) where a white arrow points to one of them], corresponding to a further small splitting in each image, which is also better observed at higher distances. Striations in couple 3-4 are only visible on images recorded with the film parallel to the direct beam, a setting which is more sensitive to misorientations (Fig. 8).

Observations of the surface of a slightly thicker crystal (1.3 mm) with the same orientation by Nomarski microscopy provide direct information on the corrugation of the surface. A typical result is shown in Fig. 9. Alternatively dark and light bands, green on the originals, roughly parallel to [001], are observed. In addition, fine striations parallel to [110] are seen in the dark bands.

Topography experiments were also performed on a thinner sample (0.18 mm), with the same orientation, $(1\bar{1}0)$. In this case, the crystal is too thin to obtain good section images. Therefore, the whole sample was illuminated, resulting in projection topographs. Important differences appeared in the low-temperature behavior: (i) The lack of well separated images, (ii) domains were observed after cooling in zero field but no clear contrast was obtained when a field was applied during the transition (case III), the only appreciable effect being the loss of visibility of the intrinsic sample defects.

V. DISCUSSION

We have identified several monoclinic twins in case III. Images 1 and 2 correspond to MFD's whose **a** and **b** axis are the same, the difference being the angle $\Delta\beta$; they are separated by a wall along (001). So do images 3 and 4. Between the MFD's corresponding to images 1 and 3, the **a** and **b** axes are interchanged, and they are separated by a (101) wall. A similar relation is found between MFD's 2 and 4.

The resulting domain configuration is complicated. Cuts by planes (110), (001), and $(1\bar{1}0)$ are represented in Fig. 10, where periodicity is assumed for simplicity. Because the domain images overlap heavily, it is not easy to determine their size from direct observation. It is however possible to determine the order of magnitude of the two distances, s and h, which characterize this model, s being the typical distance between (001) walls and h the typical perpendicular distance between (101) or $(10\bar{1})$ walls.

The vertical section topographs correspond to a virtual cut

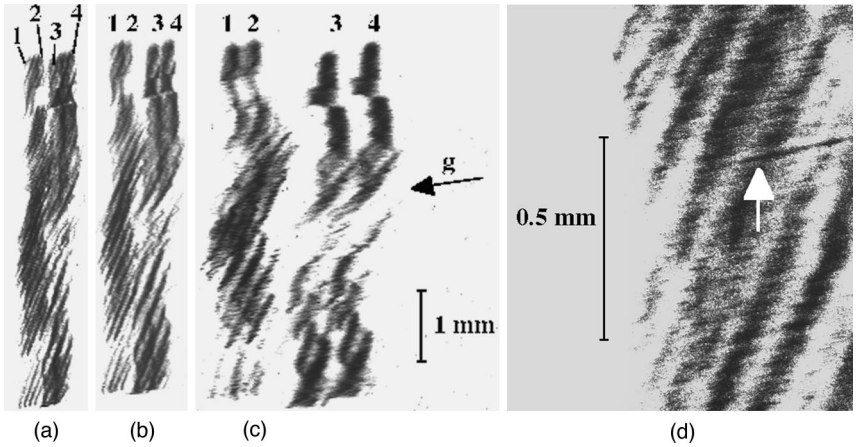

FIG. 7. White beam vertical section topographs in case III (reflection $1\bar{3}9$, $T=20$ K, $B=300$ mT, $\lambda=0.33$ Å, $\mu t\approx 1$). Three different crystal-film distances, d: (a) $d=8.5$ cm; (b) $d=14$ cm; (c) $d=42$ cm. In (d) a magnified view of (b) is shown. The white arrow indicates one streak parallel to the **g** vector.

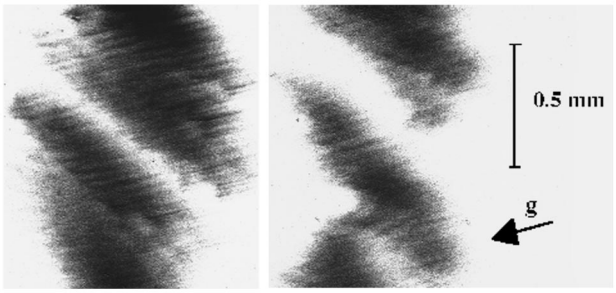

FIG. 8. White beam vertical section topograph obtained with the film parallel to the direct beam. Reflection $\overline{139}$, $T=110$ K, $B=300$ mT, $\lambda=0.4$ Å, $\mu t\approx 2$. (a) couple 1-2 (superimposed images); (b) couple 3-4 (superimposed images).

plane close to (001), the deviation being the small rotation of the sample performed with respect to the orientation where the surface would be perpendicular to the incident beam, in order to set several reflections in the Bragg position. If s was big enough, the section topographs should show only two images, 1-3 or 2-4 [Fig. 10(b)]. The fact that all of them are observed simultaneously shows that the beam actually crosses all four kinds of MFD's. This could be caused by the sample rotation ($\omega\approx 6°$) that makes the beam cross a region of width t sin $\omega\approx 80$ μm along [001]. Therefore, s is smaller than 80 μm. In addition, we observe that MFD's separated

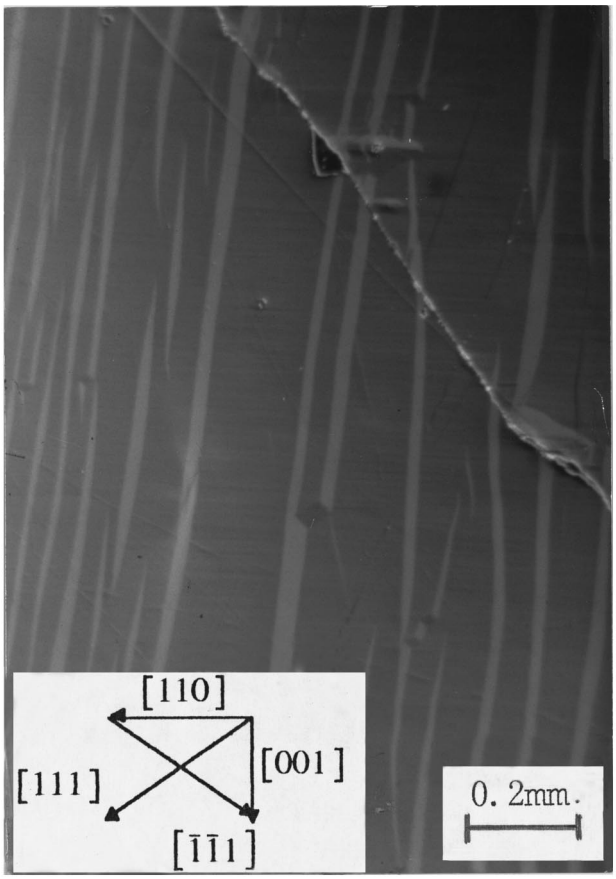

FIG. 9. Surface photography obtained by Nomarski interference microscopy ($T=80$ K, cooling in 420 mT field ∥ [001]). $(1\bar{1}0)$ sample, 4.6×4.4 mm^2, 1.3 mm thick.

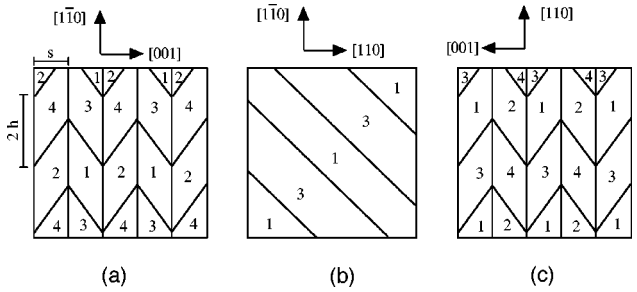

FIG. 10. Domain model for case III sections by planes (110) (a); (001) (b), and $(1\bar{1}0)$ (c).

by (001) walls give two images which are the replica of each other. This indicates that the beam intersects them at the same depth inside the sample. Otherwise, their images would appear as different and complementary in some degree, i.e., intensity in image 1 (3) would correspond to lack of intensity in image 2 (4). For this condition to be true, it would be enough if s was smaller than the slit width (20 μm).

The traces of (101) and $(10\bar{1})$ walls on (001) plane are the same and make an angle of 45° with the [110] direction [Fig. 10(b)]. This value is very close to the measured angle of 42° for the bands in Fig. 7(a). We associate these bands with MFD's 1-3 (or 2-4) intersected along the thickness. The bandwidth is related to h. From Fig. 7 h is variable but around 100 μm when taking the projection effects into account.

The misorientation between the four domains being known, it was possible to simulate the image corresponding to three different crystal-film distances. The simulations for a periodic domain structure with $s=2$ μm and $h=100$ μm are well reminiscent of the experimental results (Fig. 11), the band visibility increasing for the largest distances.

The observations by Nomarski microscopy are consistent with the above model. The s dimension being small, the intersection of the interface between couples 1-2 and 3-4 with the sample surface is a zigzag [Fig. 10(c)], on average parallel to [001]. Thus, the alternatively dark and light bands (Fig. 9) correspond to the two couples of monoclinic domains. On the other hand, calculations show that the surface plane should have the same orientation over domains 1 and 2, whereas it is expected to change over domains 3 and 4, taking on a rooflike shape. Therefore, we can assign the fine striations in the dark bands to domains 3 and 4, while the

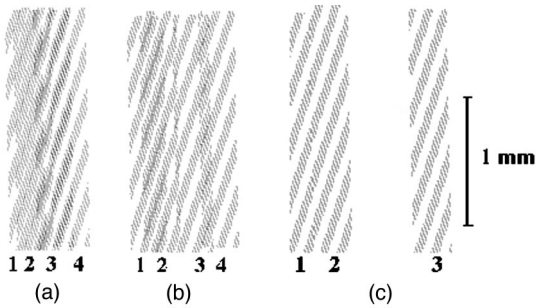

FIG. 11. Simulations of the images in Fig. 7 for three different crystal-film distances, d ($s=2$ μm, $h=100$ μm): (a) $d=8.5$ cm; (b) $d=14$ cm; (c) $d=42$ cm.

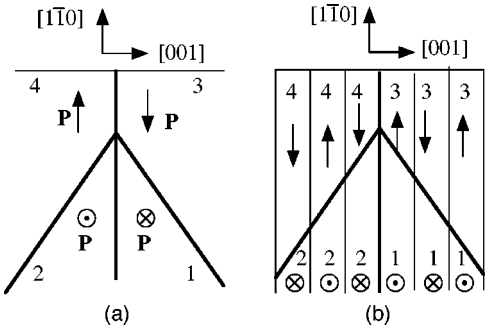

FIG. 12. Section by (110) plane showing the junction between MFD's 1, 2, 3, and 4. In (a) only one sign of the electric polarization **P** is associated to each MFD; in (b) the possibility of 180° ferroelectric walls (invisible by x-ray topography) inside each MFD. For the sake of simplicity, **P** is assumed to be along the monoclinic **a** axis.

other band (couple 1-2) does not show any internal contrast.

A picture of the monoclinic twins in the field-cooled sample (case III) thus emerges. This domain configuration is favorable from the elastic, the magnetostatic, and the electrostatic point of view:

(i) From the elastic point of view, the differences in lattice distortion between the four kinds of MFD's obtained from formulas (2), (3), and (7) fulfill the equality:

$$\Delta \frac{\partial u_i}{\partial x_j}(1-2)=\Delta \frac{\partial u_i}{\partial x_j}(1-3)+\Delta \frac{\partial u_i}{\partial x_j}(3-4) + \Delta \frac{\partial u_i}{\partial x_j}(4-2), \tag{8}$$

where the numbers between brackets indicate the couple of domains the difference in lattice distortion refers to. Strictly, the compatibility conditions discussed above [formulas (1) and (7)] are valid for two domains. Equation (8) means that compatibility between two domains is not broken by the presence of the others domains, i.e., that the junctions are Nye junctions[25] or that the whole structure has no stresses. This is consistent with the fact that no streaks, which would reveal distortions with long-range variations, are visible. It would not be true for just any set of walls between these four MFD's.

(ii) The normal component of the electric polarization can be conserved across the wall. Let $\pm[P_u,P_v,P_w]$ be the polarization in MFD 1, the $\pm$ being due to the inversion operation of the high-symmetry phase, which changes the sign of **P** without altering the strain tensor. In MFD 2 we obtain after the application of the corresponding symmetry operation a polarization $\pm[-P_u,-P_v,P_w]$. Taking the + sign in both MFD's, the normal component of the polarization is conserved through the (001) wall. Similar reasoning applies for all the walls. It is thus possible to follow a closed circuit through the four kinds of MFD's like 1-2-3-4-1 without electric charges appearing on any of the walls. Actually a unique polarization sense cannot be associated to each MFD, and there exists the possibility of having 180° ferroelectric domains, invisible by x-ray topography, inside a MFD. A picture of this conceivable situation is shown in Fig. 12 with the

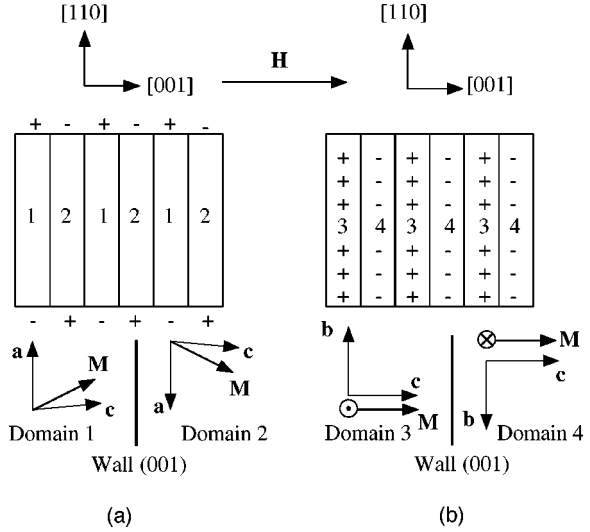

FIG. 13. Magnetic poles due to the tilting of the magnetization to the monoclinic *a* axis. (a) 1-2 couple giving rise to poles on the side surface of the sample; (b) 3-4 couple giving rise to poles on the main surface of the sample.

simplifying assumption that **P** is along the *a* axis, whereas this is only the direction of the largest component.[26,27]

(iii) The magnetization is slightly tilted to the *a* axis.[1] In MFD 1 it has the form $[M_u,M_u,M_w]$. For the experiments performed under a magnetic field only one sign is allowed due to the applied magnetic field. As before, there are no magnetic poles at the walls. However, the canting of the magnetization from the *c* axis gives rise to poles on the sample surfaces. Figure 13 shows the pole distribution, consisting of alternating + and − magnetic charges. Thus, the fine division into domains ($s<20\ \mu$m) could be an attempt to decrease the magnetostatic energy.

The above plausibility arguments do not purport to be a rigorous proof that the observed structure corresponds to minimum free energy. It should be stressed that our experiment is not sensitive to ferroelectric domains having opposite polarization and that defects usually play an important role in determining the domain configuration.

An *a priori* equivalent configuration fulfills the same elastic, electrostatic, and magnetostatic conditions, but has not been observed. In this configuration domains 1 and 2 are separated by (001) walls, and so are domains 3 and 4. The difference from the previous situation is the fact that do-

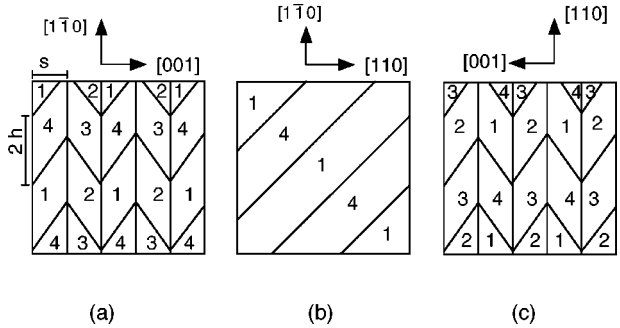

FIG. 14. The nonobserved MFD configuration equivalent (*a priori*) to the observed one (Fig. 10). Sections by planes (110) (a); (001) (b), and $(1\bar{1}0)$ (c).

mains 1 and 4 are adjacent and separated by (011) walls; domains 2 and 3 are adjacent too, being separated by $(01\bar{1})$ walls (Fig. 14).

Until now only ferroelastic monoclinic twins have been considered. They can explain the distinctly split section topographic images. However, they cannot explain the substructure visible in some of the images, e.g., the striations in Fig. 7(d) because monoclinic twins would give rise to well-separated images. Since, for the spot shown in this figure, the striations are only visible in one of the monoclinic couples (1-2), they do not correspond to parasitic contrast from dust on the slits[28] nor to intrinsic defects in the sample. Two possibilities are left: the presence of antiphase boundaries or of strictly triclinic twins. At the end of Sec. II A, it was argued that antiphase boundaries should not be observed. Furthermore, the visibility of the streaks increases with the crystal to film distance and this points to the effect of a misorientation (difference in diffraction vector **g**). Therefore, we conclude that this substructure corresponds to triclinic symmetry. The striations follow the projection of the diffraction vector **g** on the film. A geometrical reasoning indicates that the corresponding triclinic walls are perpendicular to the surface. In the twin classification used in this paper, two triclinic walls are possible inside MFD's 1 and 2: $(1\bar{1}0)$ and $(\Delta\gamma,\Delta\gamma,\sqrt{2}\Delta\alpha)$. The second one is perpendicular to the surface. Inside the images of domains 3 and 4, striations are only visible when the film is set parallel to the direct beam and again they follow the projection of the diffraction vector on the film. Two triclinic walls are allowed, (110) and $(\Delta\gamma,-\Delta\gamma,\sqrt{2}\Delta\alpha)$. The first one is perpendicular to the surface. Domains separated by triclinic walls are related by the *ac* mirror, which would still be a symmetry operation if monoclinic symmetry was retained.

Assuming that (110) triclinic walls are present in MFD's 3 and 4 and that image separations can be measured down to 0.1 mm, the fact that the triclinic twins do not give separated images sets a limit $\Delta\alpha<0.0007$ rad (0.04°). For $(\Delta\gamma,\Delta\gamma,\sqrt{2}\Delta\alpha)$ walls inside MFD's 1 and 2, calculations show that the corresponding twins should be invisible on the images corresponding to spots on the *kkl* circle of the Laue diagram, and have low visibility for other observed spots. However, this fact seems to be in contradiction with the easier observation of striations in couple 1-2.

The lack of quantitative data about the triclinic domains makes a deeper analysis difficult. The existence of (110) walls in couple 3-4 (W wall) and $(\Delta\gamma,\Delta\gamma,\sqrt{2}\Delta\alpha)$ in couple 1-2 (W' wall) is not accounted for at the present stage. The use of monochromatic beam x-ray imaging, with better crystals, should provide more information on the triclinic twins.

Some tentative explanations can be put forward on the results obtained from a thinner sample (0.18 mm). The lack of well separated images probably indicates the presence of strictly triclinic twins. The fact that, in case III, no clear contrast was observed could be due to the existence of very small domains (<5 μm) or to walls parallel to the surface. The latter are difficult to detect by projection topography, and they could conceal the intrinsic crystal defects.

VI. CONCLUSIONS

A method to analyze the image separation as a function of the spot position in a set of white-beam x-ray topographs (Laue pattern) has been developed. This method, applied to a set of section topographs, allows the identification of the twins in a sample, under the assumption that they are separated by Nye walls. In conjunction with the spatial information contained in the images, this approach made it possible to unravel the monoclinic domain structure obtained after passing the Verwey transition in a magnetic field parallel to [001]. It is favorable from the elastic, magnetostatic, and electrostatic points of view. Additional smaller distortions are detected. They cannot be associated with monoclinic twins, hence indicate that the true symmetry of magnetite in the low-temperature phase is triclinic. The thorough characterization of the corresponding triclinic twins requires a more sensitive technique, like monochromatic beam topography, as well as excellent crystals. The *in situ* application of an electric field should provide welcome insight on the ferroelectric aspects of this problem.

ACKNOWLEDGMENTS

The authors are indebted to Sakae Todo for making the crystals available, and to Toshiroh Karaki-Doy for the mechanochemical polishing of the samples.

*Present address: Departamento de Física de la Materia Condensada, Facultad de Ciencias, Universidad de Zaragoza, 50009 Zaragoza, Spain.

†Present address: 145-4 Naracho, Omiya, Saitama 331-0042, Japan.

[1] K. Abe, Y. Miyamoto, and S. Chikazumi, J. Phys. Soc. Jpn. **41**, 1894 (1976).

[2] M. Iizumi and G. Shirane, Solid State Commun. **17**, 433 (1975).

[3] J. Yoshida and S. Iida, J. Phys. Soc. Jpn. **47**, 1627 (1979).

[4] M. Iizumi, T. F. Koetzle, G. Shirane, S. Chikazumi, M. Matsui, and S. Todo, Acta Crystallogr., Sect. B: Struct. Crystallogr. Cryst. Chem. **38**, 2121 (1982).

[5] J. M. Zuo, J. C. H. Spence, and W. Petuskey, Phys. Rev. B **42**, 8451 (1990).

[6] G. T. Rado and J. M. Ferrari, Phys. Rev. B **12**, 5166 (1975).

[7] K. Siratori, E. Kita, G. Kaji, A. Tasaki, S. Kimura, I. Shindo, and K. Kohn, J. Phys. Soc. Jpn. **47**, 1779 (1979).

[8] K. Kato and S. Iida, J. Phys. Soc. Jpn. **50**, 2844 (1981).

[9] Y. Miyamoto, Ferroelectrics **161**, 117 (1994).

[10] M. Polcarová and J. Gemperlová, Phys. Status Solidi **32**, 769 (1969).

[11] M. Schlenker, P. Brissonneau, and J. P. Perrier, Bull. Soc. Fr. Mineral. Cristallogr. **91**, 653 (1968).

[12] M. Ribet, S. Léon, F. Lefaucheux, and M. C. Robert, J. Appl. Crystallogr. **23**, 277 (1990).

[13] X. R. Huang, S. S. Jiang, W. J. Liu, X. S. Wu, D. Feng, Z. G. Wang, Y. Han, and J. Y. Wang, J. Appl. Crystallogr. **29**, 371 (1996).

[14] J. F. Pétroff and A. Mathiot, Mater. Res. Bull. **9**, 319 (1974).

[15] M. Kléman and M. Schlenker, J. Appl. Phys. **43**, 3184 (1972).

[16] J. Sapriel, Phys. Rev. B **12**, 5128 (1975).

[17] *International Tables for Crystallography*, 4th revised ed., Vol. A. edited by Theo Hahn (Kluwer Academic, Dordrecht, 1995).

[18] A. Authier, Phys. Status Solidi **27**, 77 (1968).
[19] B. Capelle and C. Malgrange, J. Appl. Phys. **53**, 6762 (1982).
[20] B. Capelle, Y. Epelboin, and C. Malgrange, J. Appl. Phys. **53**, 6767 (1982).
[21] B. K. Tanner, *X-ray Diffraction Topography* (Pergamon, New York, 1976).
[22] A. R. Lang, J. Appl. Phys. **29**, 597 (1958).
[23] A. Authier, in *Diffraction and Imaging Techniques in Material Science*, edited by S. Amelinckx, R. Gevers, and J. van Landuyt (North-Holland, Amsterdam, 1978).
[24] G. Berruyer, T. Blanc, A. Filhol, and J. Laugier, OrientExpress v1, Users manual for Unix workstations, Internal report ESRF: 94BE9T/ILL:94BE11T (1994).
[25] M. Kléman, J. Appl. Phys. **45**, 1377 (1974).
[26] E. Kita, K. Siratori, K. Kohn, A. Tasaki, S. Kimura, and I. Shindo, J. Phys. Soc. Jpn. **47**, 1788 (1979).
[27] K. Kato, S. Iida, K. Yanai, and K. Mizishima, J. Magn. Magn. Mater. **31-34**, 783 (1983).
[28] P. Cloetens, R. Barrett, J. Baruchel, J. P. Guigay, and M. Schlenker, J. Phys. D **29**, 133 (1996).